

# Simulation of As-Cast Steel Ingots

Menghuai Wu,\* Andreas Ludwig, and Abdellah Kharicha

Some of the most recent examples of simulations of as-cast steel ingots are presented in this paper, focusing on discussions concerning available simulation/modeling tools and their capacities and limitations. Although, there has been some success from implementing criterion functions into commercial codes to predict shrinkage porosity and hot tearing, large-scale ingot sectioning experiments, similar to what is done a century ago, are still needed to investigate other issues, such as macrosegregation, since models are currently unable to predict such issues well. Models with more sophisticated features for macrosegregation prediction that incorporate multiphase transport phenomena are already under development. A limiting factor in application of these models for simulating steel ingots is the demand on large computation resources. Following the recent development trend and the projection of Moore's law (computer hardware), in the foreseeable future, it is predicted that multiphase models will to a great extent reduce the need for the experimental pouring-sectioning trials.

## 1. Introduction

Steel ingots have been produced since the 1870's. To understand the solidification behavior of such ingots at that time, extremely costly pouring-sectioning experiments were performed to investigate the solidification sequences,<sup>[1–4]</sup> as shown in **Figure 1a** and **b**. Several dozen ingots weighing a few hundred kilograms to several hundred tons were systematically poured and sectioned for their soundness, structural, and compositional analysis. Most fundamental knowledge about the production of steel ingots has been well established, but there are still several solidification related phenomena, which are not entirely understood. Hence, it is not surprising that even today such costly pouring-sectioning experiments are occasionally repeated.<sup>[5–9]</sup> The difference between today's experiments and those from the past is that modern analysis methods are used to obtain more structural and compositional details. One reason for repeating those experiments is to develop new alloying ingots for special applications; a more important reason is to evaluate the effectiveness of numerical models, which are believed to

replace those exhausting experiments one day. Modeling studies and numerical simulations of ingot castings have become the most economical method in this regard, but confidence in their results is still lacking.

The very first application of numerical simulation of hot metals can be dated back to the 1960's.<sup>[10]</sup> A simple heat conduction problem was solved using the finite difference method to analyze the solidification sequence in the steel ingot, as shown in **Figure 1c** and **d**. It is hardly believable that a computer from the 1960's (CPU  $\approx$ 100 kHz, memory  $\approx$ 100 kB) was able to handle the problem of ingot solidification, especially with reference to contemporary complaints about the computational capacity of modern computer hardware (CPU  $\approx$ GHz with parallel computing, memory  $\approx$ GB)! The first simulation experience for ingot casting was actually successful, and it was applied to determine the optimum delay for charging the soaking pits; it was also used to study the influence of the holding time of the ingot in the molds, and the time between stripping and charging. In the last half century, following developments in computer hardware and numerical algorithms, numerical models with varieties of simulation/modeling capacities have been developed, and applied to ingot casting practices. For example, the thermal field based solidification model has been implemented for decades in commercial codes, ProCAST<sup>[11]</sup> and MAGMASOFT,<sup>[12]</sup> and applied by metallurgists to evaluate and optimize the casting parameters, mold, and hot top design; while some other sophisticated solidification models with consideration of the multiphase transport phenomena have been developed and used to enhance the understanding of the macrosegregation mechanisms.

---

[\*] M. Wu, A. Kharicha  
Christian Doppler Laboratory for Advanced Process Simulation of  
Solidification and Melting, Montanuniversitaet Leoben, A-8700 Leoben,  
Austria  
Email: menghuai.wu@unileoben.ac.at  
A. Ludwig  
Department of Metallurgy, Montanuniversitaet Leoben, A-8700 Leoben,  
Austria

Those developments have been reviewed by different authors.<sup>[5,13–18]</sup> This article will not repeat comprehensive reviews mentioned above, but focuses on the discussions about the available simulation/modeling tools of today, their capacities and limitations. Furthermore, most recent simulation examples are presented.

## 2. Capabilities and Limitations

### 2.1. Shrinkage Cavity and Porosity

Two major shrinkage defects are observed in steel ingots: (i) macroscopic shrinkage cavity, (ii) micro porosity or pores. The macroscopic shrinkage cavity (i) appears in a form of open pipe in the hot top region. Just below the pipe there occasionally exist disconnected satellite cavities. The sinking of the melt level due to the accumulated volume shrinkage by the melt cooling and solidification leads to the formation of a funnel-shape pipe. A formation mechanism of the satellite cavities is similar to the open pipe; the only difference is that they form in some isolated regions, which are disconnected from the open pipe.



Prof. Menghuai Wu received his Master degree in 1986 from the Northwestern Polytechnical University in China, PhD degree in 2000 from the Foundry Institute, RWTH Aachen in Germany, and Habilitation (professorial certificate) in 2008 from the Montanuniversitaet Leoben in Austria, and became the head of Christian Doppler Laboratory for “Advanced Process Simulation of Solidification and Melting” in 2010. His main research interests are the modeling and simulation of solidification and related phenomena during different casting process.

Within each isolated melt region, the feeding flow is still active. These isolated melt regions are caused by improper design of hot top or by the so-called “bridging” effect. Numerical treatment of this kind of macroscopic shrinkage cavities is to accumulate shrinkage volume in each isolated melt region and relocate the shrinkage volume based on thermal and gravity fields.<sup>[19,20]</sup> Micro porosity (ii) appears mostly in the centerline region of the ingots. During the

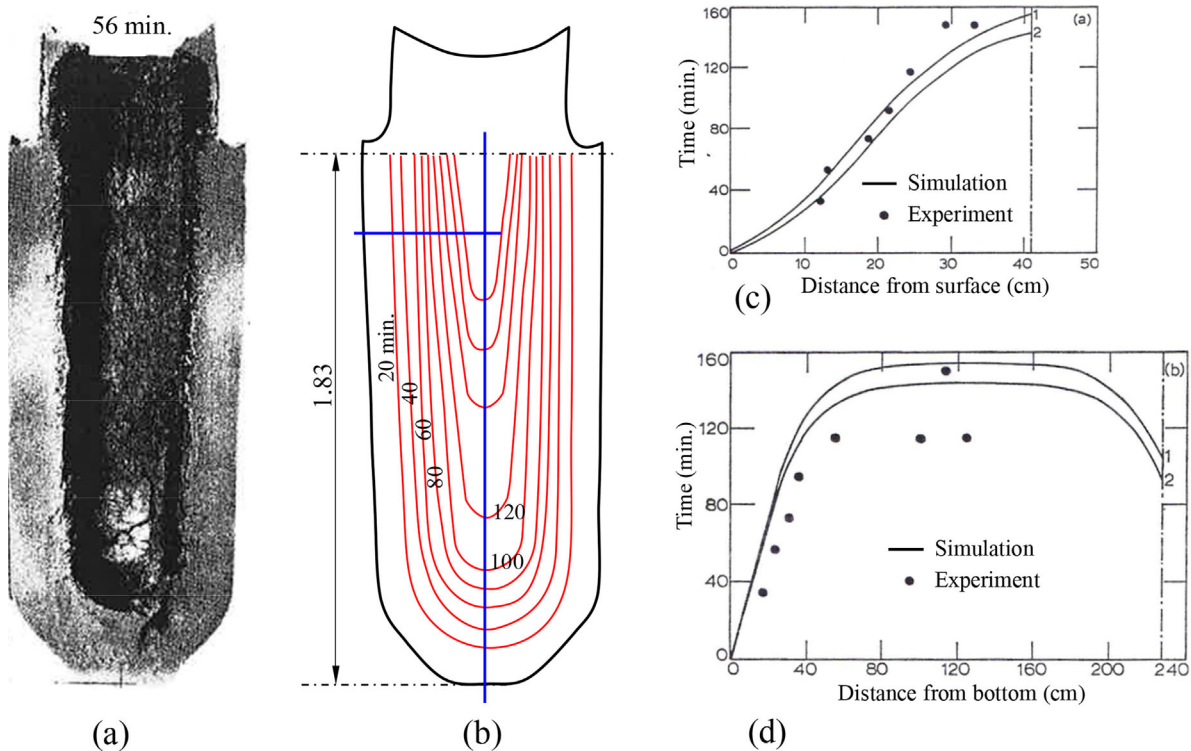


**Figure 1.** Experimental (pouring-dumping-sectioning) study of the solidification sequence in a 10 ton ingot ( $0.82 \times 0.82 \text{ m}^2$  square section) and comparison with numerical simulation. a) Partially solidified steel ingots were dumped (6 ingots dumped at 34, 56, 73, 94, 118, 150 min.) and the remained solid shell were sectioned to investigate the solidification sequence; b) reconstructed solidification sequence by extrapolation of the dumping ingots; c), d) numerically calculated solidification front along the transverse section and along the centerline vertically, in comparison with the dumping experiment (simulation curve 1: pouring temperature of  $1600 \text{ }^\circ\text{C}$ , simulation curve 2: pouring temperature of  $1530 \text{ }^\circ\text{C}$ ). Figures are reproduced from refs.[2,10]

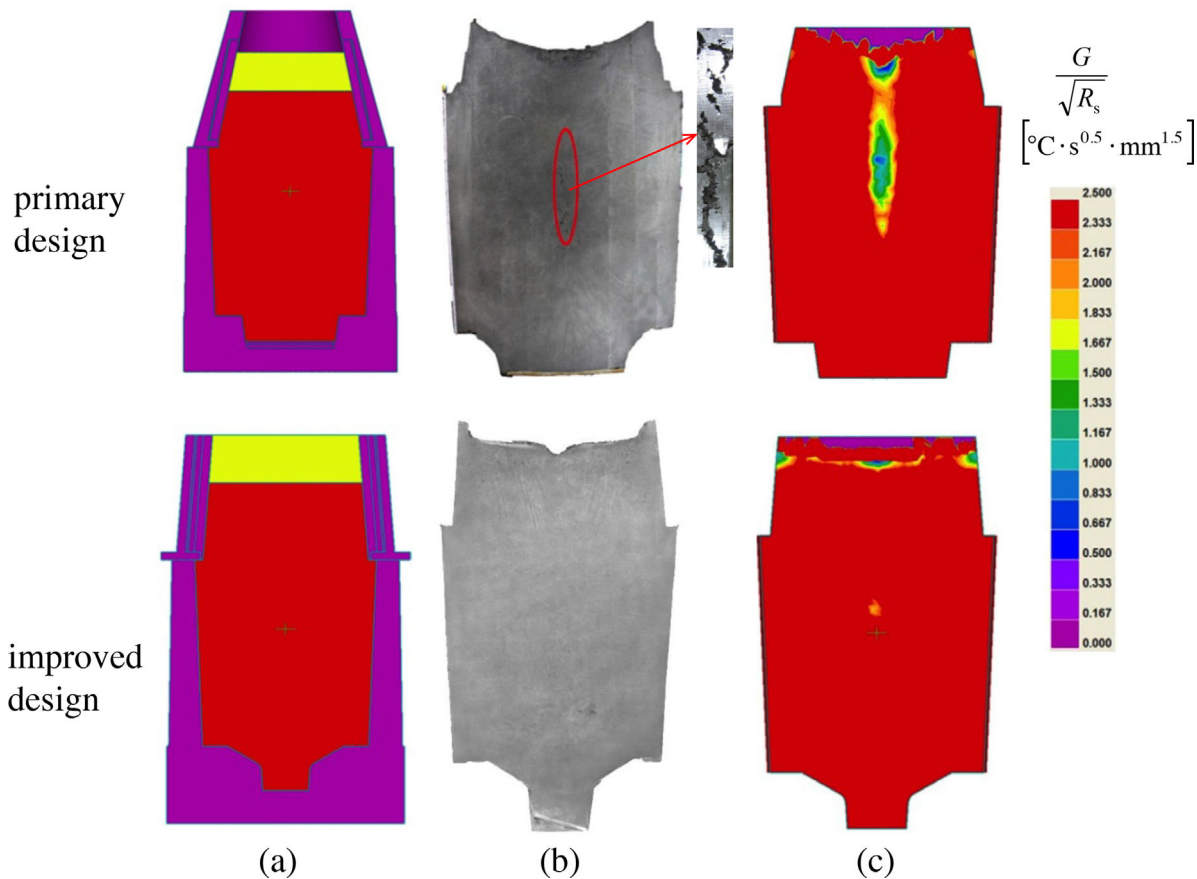


**Figure 2.** Application of numerical simulation to minimize the shrinkage defects by improving the ingot design (100-ton steel ingot, 30Cr<sub>2</sub>Ni<sub>4</sub>MoV). a) Primary and improved ingot designs; b) both ingots were cast and sectioned for metallographic analysis: centerline porosity was detected for the original ingot design, while a sound ingot was obtained for the improved design; c) numerically predicted shrinkage pipe (profile of the top surface) and centerline shrinkage porosity as predicted by a criterion function  $G/\sqrt{R_s}$ , where  $G$  is the temperature gradient and  $R_s$  is the solidification rate (moving speed of the isotherm). The simulation-experiment agreement is satisfactory. The simulations were performed with a commercial software ProCAST,<sup>[11]</sup> figures were reproduced from refs.[6,24]

late stage of solidification, the deep interdendritic mushy zone along the centerline is difficult to feed by the melt coming from the hot top. When the shrinkage-induced pressure drop reaches a threshold, pores would initiate and grow. Some criterion functions merely based on the thermal field, for example, the Niyama criterion,<sup>[21]</sup> have been derived to predict the occurrence probability of the shrinkage porosity. This idea was later modified<sup>[6]</sup> or extended by considering the effect of mush zone morphology and permeability.<sup>[22]</sup> Models for both macroscopic and microscopic shrinkage defects have been implemented in ProCAST<sup>[11]</sup> and MAGMASOFT,<sup>[12]</sup> some successes were achieved to minimize the shrinkage defects in steel ingots by improving the casting design.<sup>[6,23–26]</sup> One example is shown in Figure 2.<sup>[6,24]</sup>

Most commercial or in-house codes for calculation of shrinkage defects are based on the transient thermal field during solidification, and it is also true that the governing phenomenon for shrinkage defects is the global solidification sequence, which depends mainly on the thermal field.

Mold filling can be included in the calculation, but for most conventional ingots the mold filling takes only 1–2% of the while solidification time of the ingot. The crucial factor for the simulation accuracy is the material data (thermal physical and thermodynamic), and the interface heat transfer coefficients between the casting and different mold materials. Providing reliable data are imputed for these parameters, a reasonable simulation-experiment agreement can be achieved (Figure 2). The requirements on the computer hardware are low, and a contemporary PC with standard configuration would be sufficient for most calculations. Therefore, a numerical proof of shrinkage defects is possible and highly recommended for each newly-designed ingot.

Shrinkage simulation based purely on thermal field has the following limitations. Solidification with mixed columnar-equiaxed structure, multiphase flow, and the formation of macrosegregation are not considered. Equiaxed crystal sedimentation will alter the global solidification sequence; it should have an influence on the final

distribution of the macroscopic shrinkage cavities. The criterion functions, as derived on the base of the columnar solidification, might not be valid for the equiaxed solidification.

## 2.2. Stress and Strain

Surface and internal cracks have been traditionally often found in steel ingots. As early as the 1980s, a 2-dimensional finite-element elasto-viscoplastic thermal mechanical model<sup>[27]</sup> was used to investigate the mid-face<sup>[28]</sup> and off-corner panel (surface) cracks<sup>[29]</sup> in steel ingots. The thermal behavior during solidification, subsequent cooling after stripping, and reheating after charging into soaking pit was calculated in advance, and then used as input data for the thermal-mechanical model to calculate the displacement, stress, and strain in the cross section of the ingot. By analyzing the local extremes of the tensile or compressive stress in some critical regions and at some critical moments, the knowledge about the formation of the mid-face and off-corner panel cracks was obtained, and on this base some counter measures were suggested to reduce this kind of cracks in as-cast ingots. Cracks as formed in/near the ingot center are mostly regarded as examples of hot tearing,<sup>[30]</sup> which arises from a complex combination of thermal mechanical and solidification phenomena.<sup>[31,32]</sup> This kind of defect is basically associated with the incomplete melt feeding and tensile

deformation as generated in a coherent region of the mushy zone (solid fraction  $f_s$  between 0.9 and 0.99), which is also evaluated by a so-called brittle temperature range (BTR), i.e., the temperature range between the coherent temperature and the zero ductility temperature. Both strength and ductility of the material drop rapidly in the BTR; the coherent dendrite network can be pulled apart by tensile deformation, while the mush is impermeable and feeding becomes impossible. Any favorite location of crack, for example, void or pore, would propagate along the liquid film of grain boundary to develop as the final form of hot tear. Direct simulation of the hot tearing in steel is difficult, but some criterion functions were developed to estimate the hot tearing susceptibility, for example, thermal field based Clyne-Davies criterion,<sup>[33]</sup> thermal-and-mechanics based WYSO criterion.<sup>[34]</sup> They are implemented in commercial software, for example, ProCAST,<sup>[11]</sup> THERCAST (trademark of TRANSVLOR S.A., France).<sup>[35]</sup> A simulation example is shown in Figure 3.

Modeling thermal mechanical defects in steel ingots is not as mature a technique as modeling shrinkage defects. The major challenges for calculating thermal stress and strain during solidification are the broad temperature range, which spans different material laws (pure fluid mechanics, visco-plastic, elasto-viscoplastic), and the shortage of material data at an elevated temperature. What makes the problem more complex is solid state phase transformation,<sup>[27-29]</sup> nucleation of cracks or tears from other defects like pores,<sup>[30]</sup> and the feeding flow

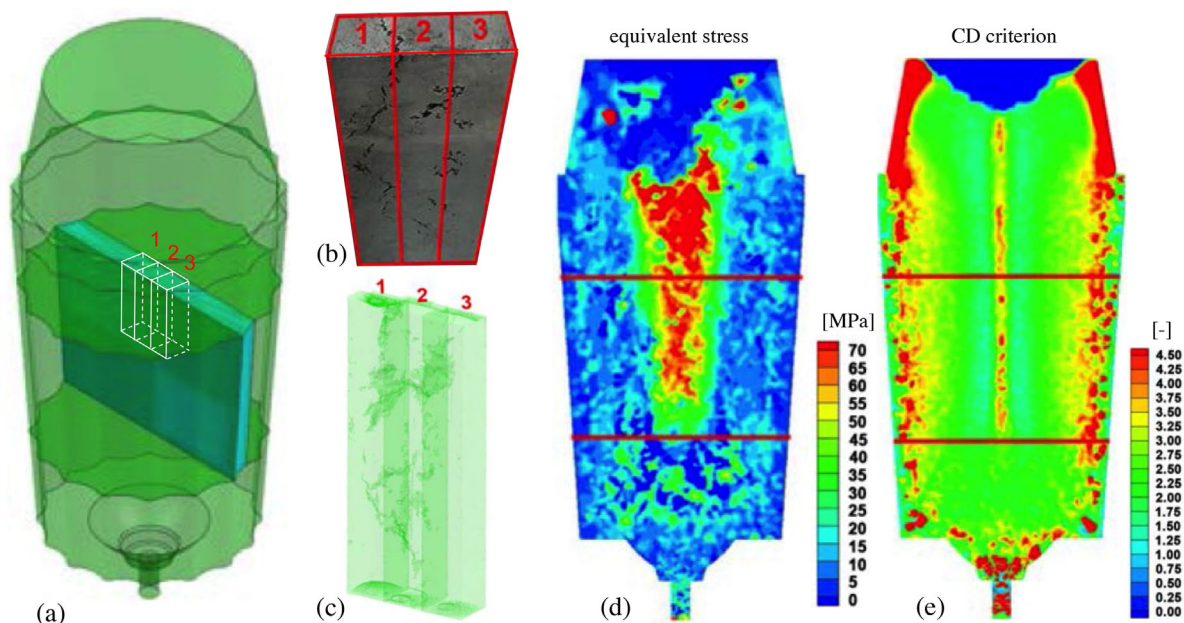


**Figure 3.** Susceptibility of the internal crack-like defect in a 6-ton steel ingot. a) Schematic of the ingot geometry; b) the as-cast ingot was sliced longitudinally near the casting center; c) the sliced samples were examined by a high energy 3D X-ray computer tomography for the internal crack and pores; d) numerical calculation of the equivalent stress, as built during cooling through the BTR; e) CD (Clyne-Davies) criterion function, as susceptibility indicator for the hot tearing (internal crack). The simulations were performed with a commercial software ProCAST,<sup>[11]</sup> figures were reproduced from refs.[30]

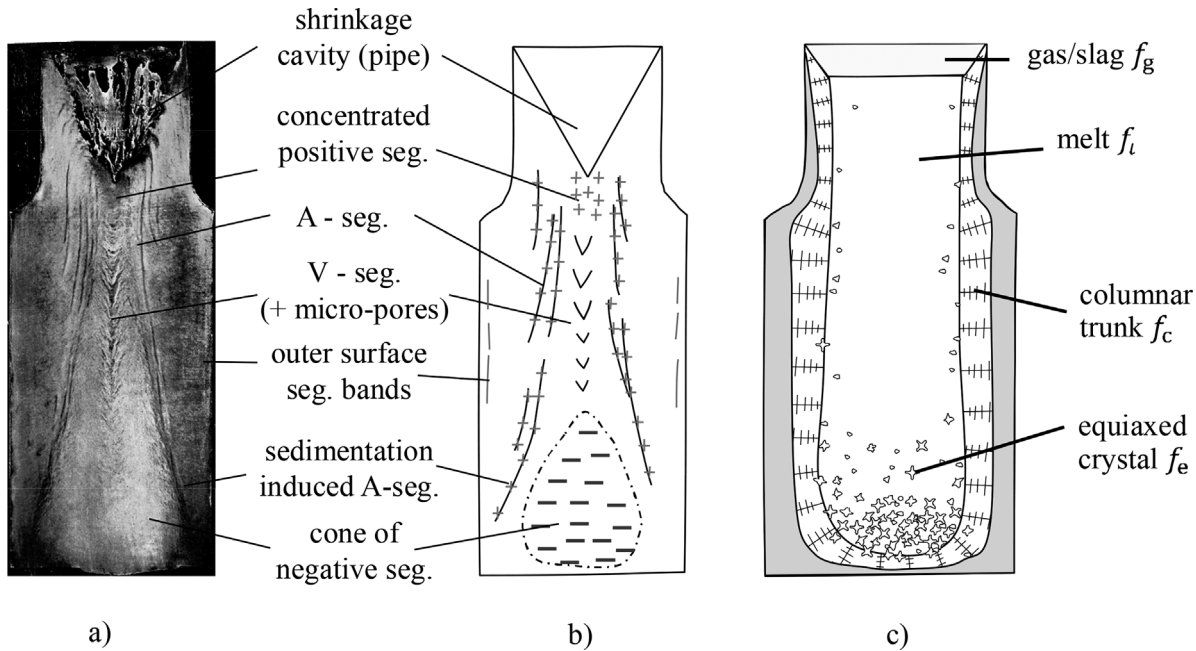


**Figure 4.** Typical macrosegregation pattern as observed in steel ingots. a) Sulfur print of a 10.5-ton steel ingot with nominal composition of 0.30 wt% C<sup>[11]</sup>; b) schematic description of the different types of macrosegregation; c) schematic of the solidification process and involved phases (melt, columnar, equiaxed, covering slag).<sup>[36]</sup>

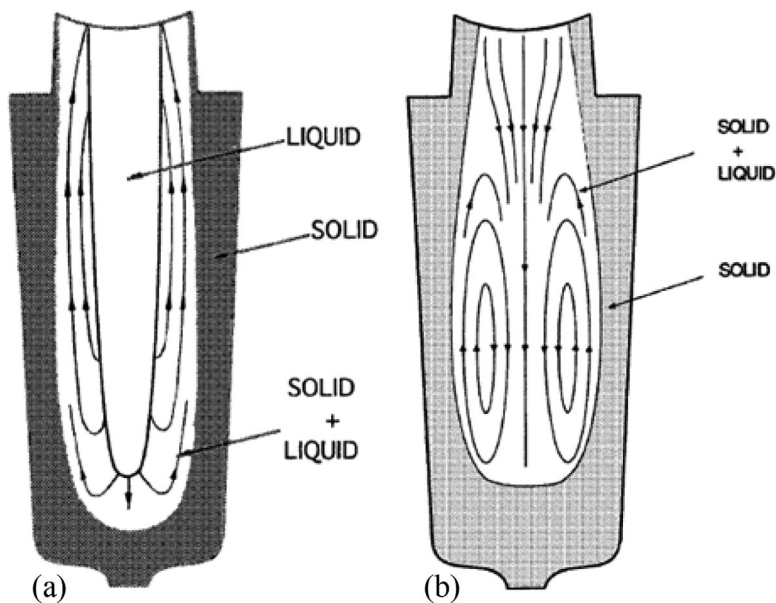


**Figure 5.** Schematic diagram of flow lines, which would lead to the main forms of macrosegregation, as observed in ingot solidification: a) central fully liquid zone present, b) later stage of solidification.<sup>[15]</sup> With the LSRE theory,<sup>[37]</sup> the result of upward flow in the liquid-solid (mushy) region is positive segregation at the center and upper regions of the ingot; the upward interdendritic flow at the bottom of the ingot, being down a temperature gradient must result in negative segregation in this region; in the middle-radius region along the flow path, A-segregates may result, when a local remelting condition (the flow velocity component in the temperature gradient direction is larger than the moving speed of isotherm) is fulfilled. Picture is taken from ref.[15] with permission.

Models	Short descriptions of key features	Refs.
Mixture continuum solidification model	<ul style="list-style-type: none"> <li>- One phase (quasi two phases);</li> <li>- Mixture continuum to treat the mushy zone;</li> <li>- Enthalpy-based solidification model;</li> <li>- Evolution of solid phase according to a predefined <math>f_s - T</math> relation;</li> <li>- Permeability law for the interdendritic flow;</li> <li>- Species transport with melt flow only.</li> </ul>	[38–49]
Two-phase globular equiaxed solidification model	<ul style="list-style-type: none"> <li>- Two phases: melt and equiaxed crystal;</li> <li>- Spherical morphology for the equiaxed crystal;</li> <li>- Diffusion-governed crystal growth;</li> <li>- Flotation and sedimentation of equiaxed crystals (e.g., buoyancy and drag law);</li> <li>- Species transport with melt flow and crystal sedimentation.</li> </ul>	[50–57]
Two-phase cylindrical columnar solidification model	<ul style="list-style-type: none"> <li>- Two phases: melt and columnar trunk;</li> <li>- Cylindrical morphology for the columnar trunk;</li> <li>- Diffusion-governed crystal growth;</li> <li>- Interdendritic flow (permeability law);</li> <li>- Species transport with melt flow only.</li> </ul>	[58–65]
Three-phase mixed columnar-equiaxed solidification model (non-dendritic)	<ul style="list-style-type: none"> <li>- Three phases: melt, equiaxed crystal and columnar trunk;</li> <li>- Cylindrical crystal morphology for columnar, spherical for equiaxed;</li> <li>- Columnar tip tracking;</li> <li>- Diffusion-governed crystal growth;</li> <li>- Interdendritic flow &amp; grain sedimentation;</li> <li>- Species transport with melt flow and crystal sedimentation;</li> <li>- Columnar-to-equiaxed transition.</li> </ul>	[66–71]
Four-phase mixed columnar-equiaxed solidification model (concurrent macrosegregation and shrinkage cavity)	<p>All other features are the same as the above “three mixed columnar-equiaxed solidification model”, but a 4th phase (covering liquid slag or gas phase) is considered to feed the accumulated solidification shrinkage. The concomitant formation of the shrinkage cavity and macrosegregation is simulated in a coupled manner. Additionally, following features are considered:</p> <ul style="list-style-type: none"> <li>- A simplified dendritic model for equiaxed solidification;</li> <li>- CBN (Carlson-Beckermann-Niyama) criterion<sup>[22]</sup> for the centerline shrinkage porosity.</li> </ul>	[36]

**Table 1.** Overview of macrosegregation models.

through the coherent dendrite network. A thermal mechanical model considering different material laws and incorporating above solidification related phenomena does not exist and further research is needed.

### 2.3. Macrosegregation

Different types of macrosegregation were observed in steel ingots (Figure 4a,b): a concentrated positive segregation below the shrinkage cavity (pipe); a cone-shaped, negative segregation in the bottom region, a crystal sedimentation induced A-shape segregation band as located slightly above the bottom equiaxed zone; A-segregates in the middle-radius region of the columnar or branched columnar structure zone; V-segregation along the centerline, light segregation bands upon careful etching near outer surface. Despite nearly one century's worth of studies on this topic,<sup>[1,2,13]</sup> a quantitative explanation of the macrosegregation formation was not possible until the 1960s – Fleming's masterpiece.<sup>[37]</sup> It was understood<sup>[15]</sup> that "all types of macrosegregation form within the liquid-solid zone, not in front of it; in most cases, it is the result of slow interdendritic flow, driven by shrinkage, geometry,

solid deformation or gravity." In the case of carbon steels, the density of interdendritic melt generally decreases during solidification, presumably resulting in the flow pattern of Figure 5. This helps to explain the top concentrated positive segregation, bottom negative segregation zone, and to some extent indirectly the formation of A-segregates according to the so-called LSRE (local solute redistribution equation) theory.<sup>[37]</sup> If the solute-concentrated liquid rises and flows to warmer parts of the ingot, it would be a normal case that the flow crosses isotherms, leading to remelting, and channel formation, i.e., A-segregates. Unfortunately, the previous theory cannot explain all macrosegregation mechanisms as related to the multiphase transport phenomena (Figure 4c), especially crystal sedimentation.

Improving the previous knowledge about macrosegregation by using numerical models has been the research goal of the last two decades. Models, applicable for the calculation of macrosegregation of industrial ingots, are summarized in Table 1. For the reason of computational efficiency, the one-phase mixture solidification model,<sup>[38–49]</sup> or two-phase model considering either stationary solid (columnar) or moving solid (equiaxed)<sup>[50–65]</sup> are preferred. In order to consider both columnar and equiaxed phases

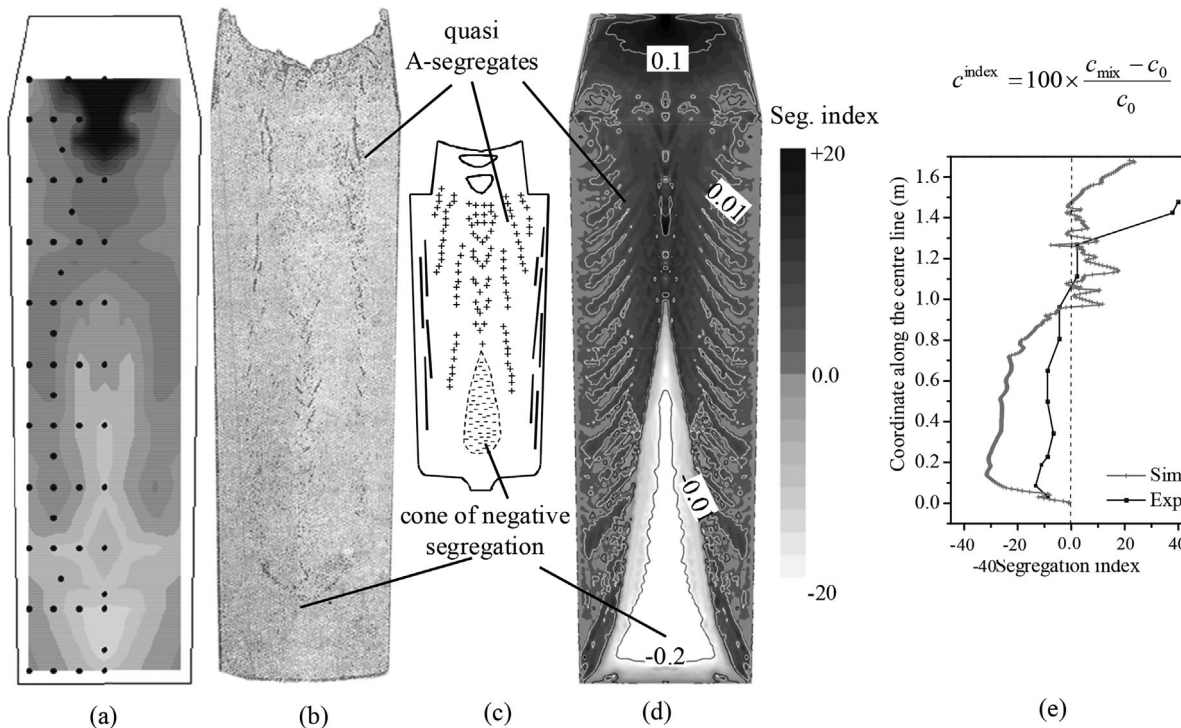


**Figure 6.** A three-phase mixed columnar-equiaxed solidification model<sup>[67]</sup> is used to simulate macrosegregation in a 2.45-ton ingot.<sup>[69]</sup> a) Reconstructed segregation map in gray scale (black for the positive segregation and light for the negative segregation) out of chemical analysis of 54 drilling samples; b) sulfur print of the as-cast ingot<sup>[1]</sup>; c) schematic of the typical macrosegregation pattern in steel ingots; d) simulated macrosegregation in gray scale overlapped with isolines; e) comparison of the numerically simulated macrosegregation with the experiment along the ingot centerline. The macrosegregation, both experimental a) and simulated d), e), is shown for the segregation index ( $c^{\text{index}} = 100 \times (c_{\text{mix}} - c_0) / c_0$ ). The calculation was performed in 2D axis symmetry with an average grid size of 5 mm. Picture is taken from ref.[69] with permission.

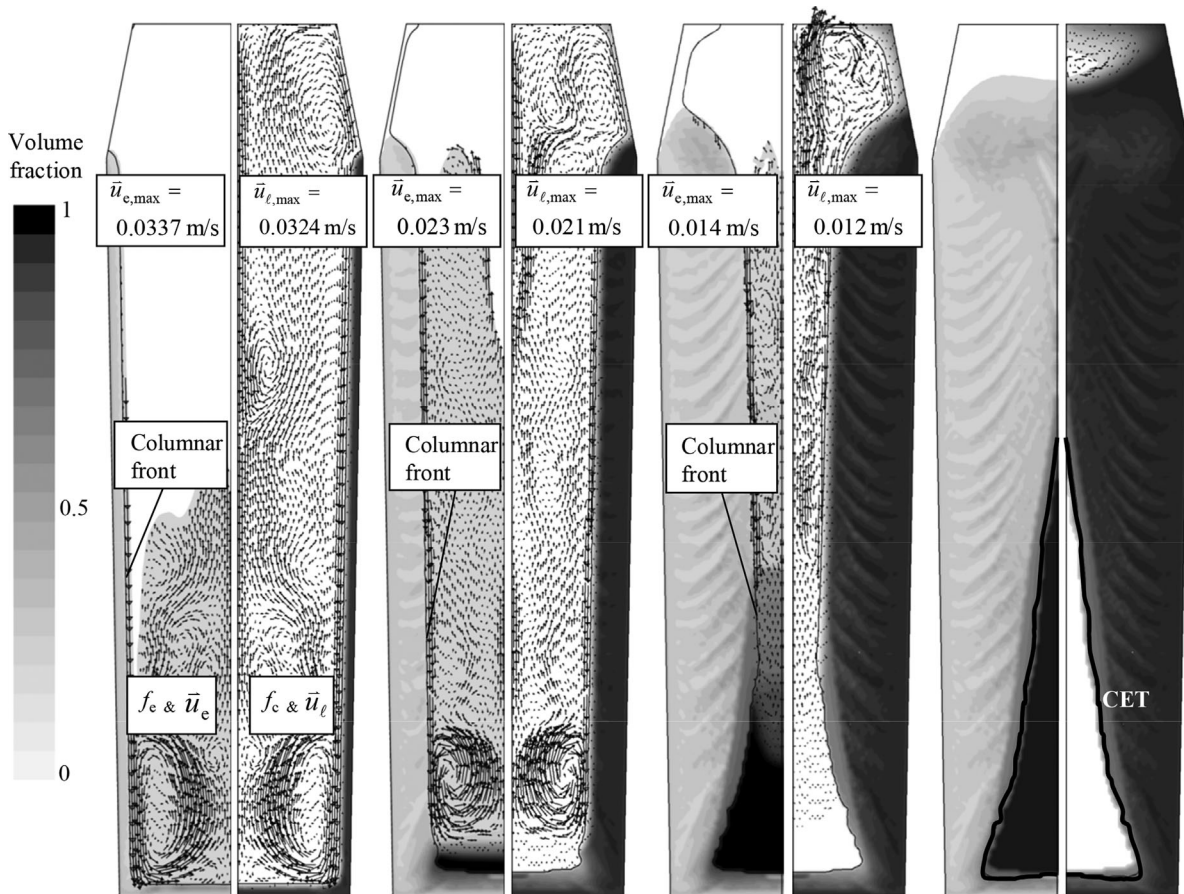


**Figure 7.** The solidification sequence of the 2.45-ton ingot (Figure 6) at 100, 500, 1500, and 4000 s. The solidification process is described with the phase volume fractions (columnar  $f_c$  and equiaxed  $f_e$ ) and the velocity fields (liquid melt  $\bar{u}_e$  and equiaxed  $\bar{u}_l$ ). The volume fraction of each phase is shown in gray map with 20 gray levels from 0 (white) to 1 (black). The left half of each graphic shows the evolution of the equiaxed volume fraction ( $f_e$ ) and the equiaxed sedimentation velocity ( $\bar{u}_e$ ), indicated by the black arrows. The right half of each graphic shows the evolution of the columnar volume fraction ( $f_c$ ) and the melt velocity ( $\bar{u}_l$ ), indicated by the black arrows. The position of the columnar dendrite tip is marked with a black solid line. The picture has been taken from ref.[69] with permission.

simultaneously, a model considering 3 phases was developed<sup>[66–68]</sup> and applied for calculation of industrial ingots. Most recently, a four phase model has been proposed to treat the complex solidification process as depicted in Figure 4c, with the ultimate goal to simulate both macrosegregation and shrinkage cavity/porosity in the coupled manner.<sup>[36]</sup>

A simulation example for a 2.45-ton steel ingot with the three-phase mixed columnar-equiaxed solidification model<sup>[69]</sup> is presented in Figure 6 and 7. As both columnar and equiaxed structures are considered, most important macrosegregation phenomena can be “reproduced” numerically: the formation of the concentrated positive segregation in the hot top, a conic negative segregation in the bottom equiaxed zone, some quasi-A segregation bands (corresponding the A-segregates) in the middle radius region. The complex of multiphase flow dynamics leads to the final distribution of macrosegregation. The calculated solidification sequence and the multiphase flow

pattern, Figure 7, are by no means stable, as previously presumed (Figure 5). The melt flow in the bulk region ahead of the columnar dendrite tip front is driven by different mechanisms: the solutal buoyancy driving upwards; the thermal buoyancy driving downwards; the equiaxed sedimentation dragging the surrounding melt downwards, and even some others, for example, shrinkage-induced feeding flow. Generally, the two downward driving forces dominate, and the melt flows downwards along the columnar dendrite tip front. This downward flow along the columnar tips will push the melt to rise toward the ingot center. This rising melt will interact with the falling equiaxed crystals and with the downward flow near the columnar tip front, to form many local convection cells. The pattern of melt convection and crystal sedimentation becomes chaotic. These local convection cells develop or they are suppressed dynamically, and the flow direction in the cells changes with time. One striking feature of the three-phase solidification model is the

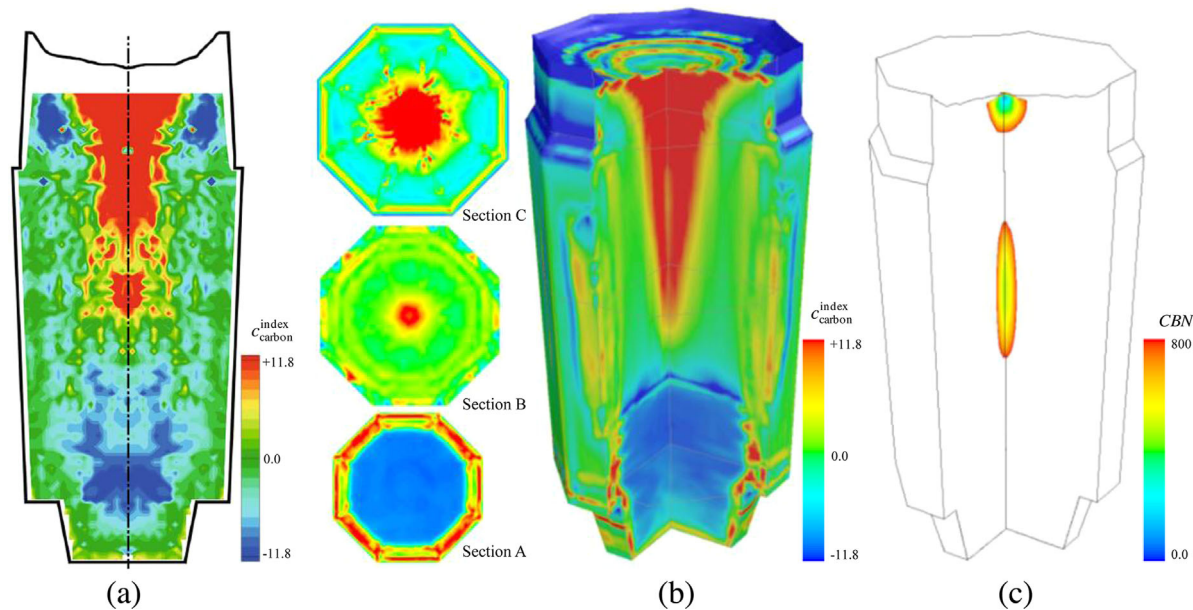


**Figure 8.** A four-phase mixed columnar-equiaxed solidification model is used to simulate macrosegregation in a 36-ton ingot. a) The macrosegregation map of the as-cast ingot in the longitudinal section was determined chemically using infrared carbon-sulfur analyzer (only half of the section was analyzed, another half is mirrored)<sup>[73,74]</sup>; (b) Numerically-simulated segregation maps in different vertical and horizontal sections, as presented in the similar color scale as the experiment; (c) as-predicted shrinkage cavity (top surface profile) and probability of the centerline shrinkage porosity according to the CBN-criterion.<sup>[22]</sup> The macrosegregation, both experimental a) and simulated b), is shown for the carbon segregation index ( $c_{\text{carbon}}^{\text{index}} = 100 \times (c_{\text{mix}} - c_0) / c_0$ ).

consideration of the mixed columnar-equiaxed solidification and the CET (columnar-to-equiaxed transition). It is a widely accepted fact that segregation behavior in steel ingots is closely related to a concurrently growing crystal structure.<sup>[17,72]</sup> The predicted global segregation pattern (Figure 6c) agrees reasonably with the experiment (Figure 6a,b), but there is still a quite large discrepancy between them, if we closely look at the segregation profile along the centerline (Figure 6e). One reason for this discrepancy is due to the assumed globular-equiaxed crystal morphology, which leads to an overestimation of the sedimentation-induced negative segregation. Some other reasons are neglecting the interaction with the formation of shrinkage cavity and porosity, the lack of proper prediction of the A-segregates, and the lack of reliable process parameters of the historic ingot. This simulation (2D axis symmetrical) took 2 weeks on an 8-core cluster (8 × 2.93 GHz).

Simulation of a 36-ton ingot has been made with a four-phase mixed columnar-equiaxed solidification model, as shown **Figure 8–10**. Major improvements of the model in comparison with the previous three-phase models are: (i) including the dendritic morphology of the equiaxed crystals, (ii) including the solidification shrinkage and its interaction with the formation of macrosegregation. It is worth mentioning that the casting was recently made, and more reliable process conditions and precise segregation measurement of the as-cast ingot were provided.<sup>[73,74]</sup> The result was a very

promising simulation-experiment agreement, either regarding the segregation map (Figure 8) or the segregation profiles along different lines (Figure 9). It also provides reasonable shrinkage cavity and porosity information. The macrosegregation distribution map in the ingot itself is not axisymmetric. The experimentally-determined segregation map was measured for each half section, and mirrored. This non-axisymmetric segregation pattern is caused by the dynamics of the multiphase flow, as demonstrated in **Figure 10**. Although a relatively coarse mesh ( $\approx 2.2$  cm) is used for the current simulation – and with such a coarse grid – it is difficult to calculate the A-segregates (channel segregation), the modeling result, Figure 8b Section C, does show a strong tendency of A-segregates in the upper part of the ingot. A detailed analysis of segregation mechanisms of different types, based on the dynamic solidification process and the multiphase flow, can refer to previous publications.<sup>[36,69]</sup>

One shortcoming of most multiphase macrosegregation models is the high calculation cost. The above calculation example in full 3D with the four-phase solidification model took  $\approx 4$  weeks in parallel on 12 cores (2.9 GHz). One reason is the large tonnage of the ingot and the long solidification time (7.6 h), but the main reason is the sophisticated non-linear coupling of the multiple equation system. Twenty-one transport equations were solved simultaneously. Despite the long calculation time, the grid resolution (average grid size of

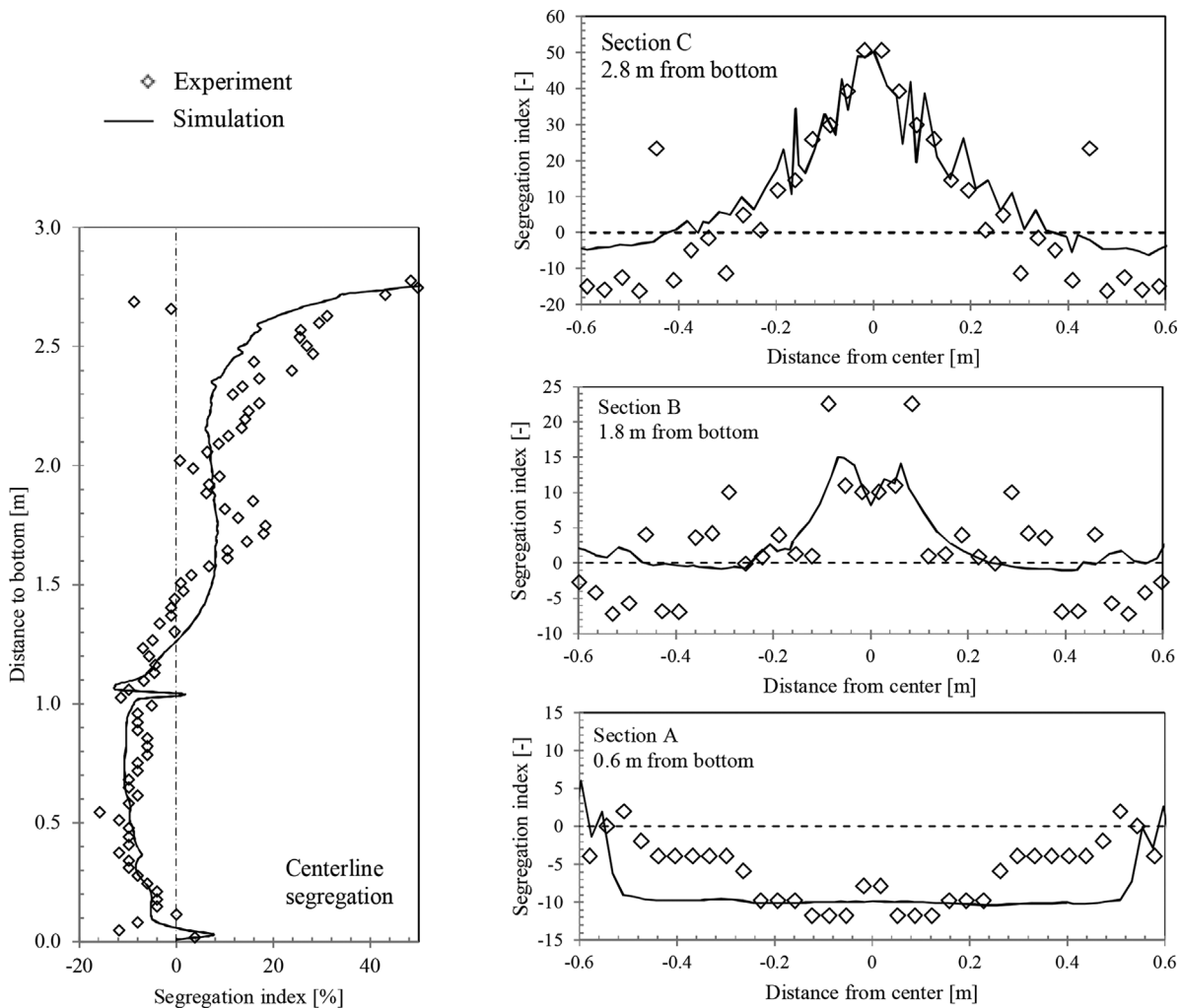
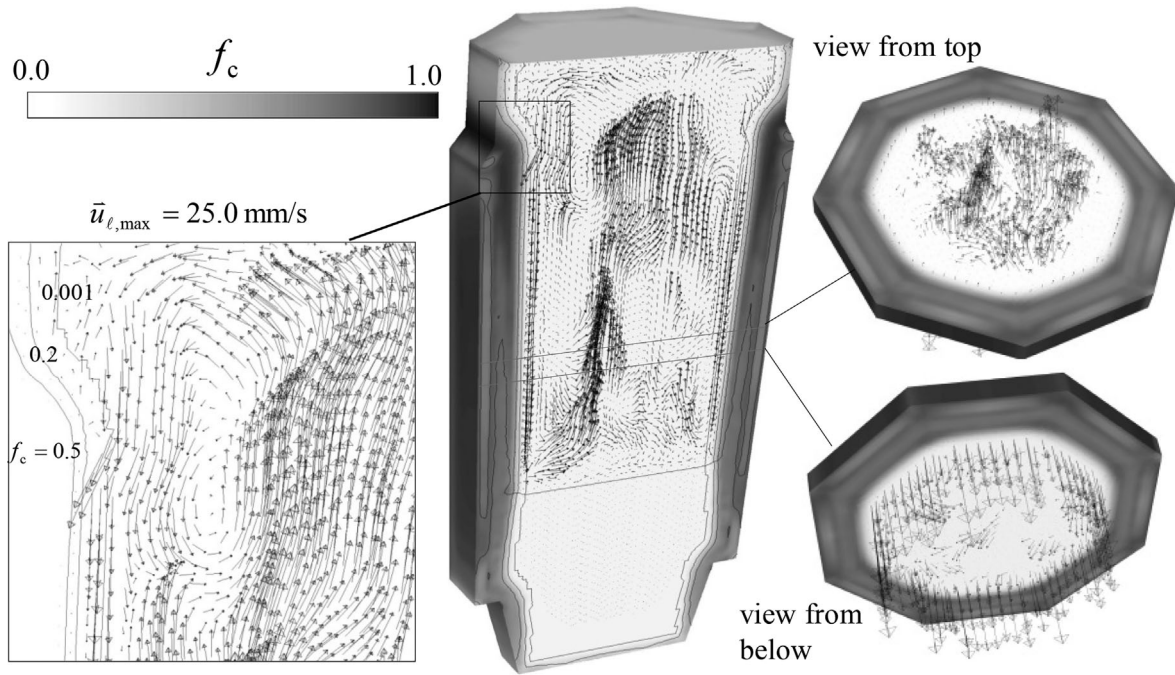


**Figure 9.** Comparison of the numerically-simulated macrosegregation profiles along the centerline (left) and along the diameter of three different horizontal sections (right: see Section A, B, C in **Figure 8b**) with the experimental specimen (36-ton ingot). Data from the experiment have been taken from ref.[73] with permission.

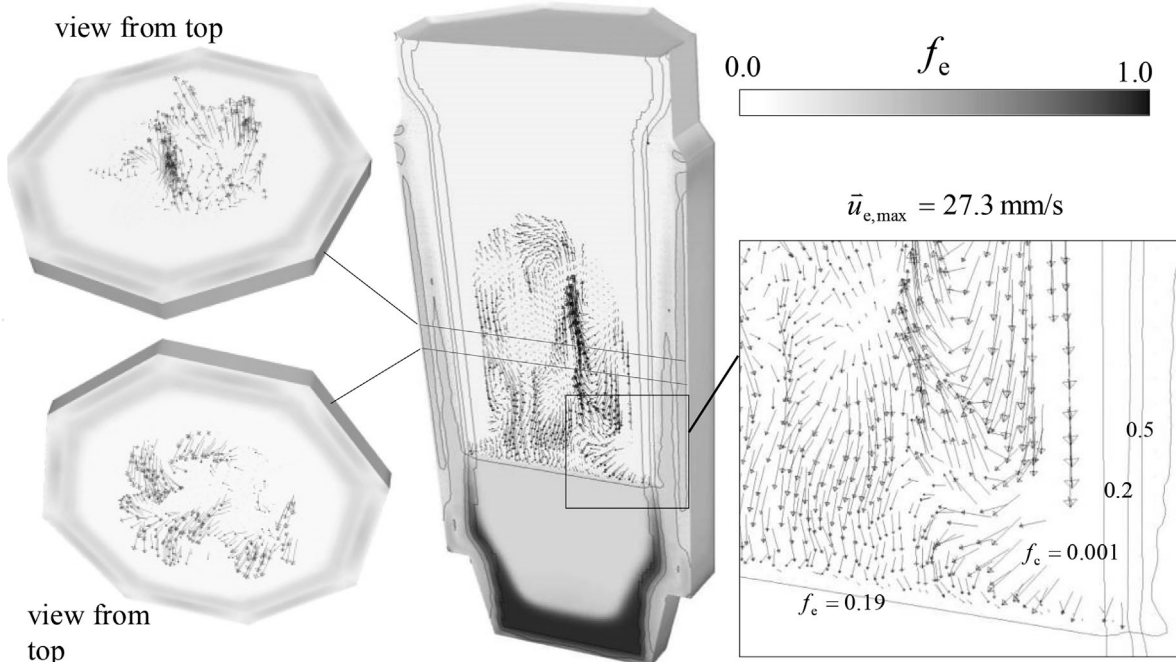
2.2 cm) is still not sufficient to obtain the A-segregates or quasi A-segregates. A grid size of  $\approx 1$  mm is normally required to get the pipe/laminar channel structure of A-segregates.<sup>[64,65]</sup> This is not feasible for an industrial ingot with the today's computer hardware. The mixture continuum solidification model contains fewer equations and it is computationally more efficient, but some important features for the macrosegregation formation are missing. These features include: crystal sedimentation, diffusion-governed growth kinetics, mixed columnar-equiaxed structure and CET (columnar-to-equiaxed transition), concurrent formation of macrosegregation and shrinkage cavity. Even with such a simple model, it would still take days or a week to run a simulation for an industrial scale ingot.

One alternative solution with some thermal field based criterion functions (e.g., Rayleigh-number criterion<sup>[75,76]</sup> and Suzuki criterion<sup>[77]</sup>) was also suggested for

the onset condition of channel segregation. The simulations with those criteria are computationally most efficient, they take only hours or less than a day. However, the critical values of those criteria for the A-segregate to occur depend on the alloy composition, the ingot geometry, the density change of the saturated interdendritic melt, and even the casting direction.<sup>[13]</sup> It means that an experimental determination or calibration of the critical values is mostly required for each special case. Additionally, a recent study shows that the onset criterion is not sufficient to predict the A-segregates, as the stabilization of the channel by the growth of the channel is governed by the flow-solidification interaction near the solidification front.<sup>[64,65,78]</sup> The base segregation – like the concentrated positive segregation in the hot top and the sedimentation induced bottom negative segregation – cannot be calculated with the criterion functions.



a)  $f_c$  and  $\bar{u}_l$



b)  $f_e$  and  $\bar{u}_e$

**Figure 10.** The solidification sequence of the 36-ton ingot, as an example, at 2530 s. The solidification process is described with the phase volume fractions (columnar  $f_c$  and equiaxed  $f_e$ ) and the velocity fields (liquid melt  $\bar{u}_l$  and equiaxed  $\bar{u}_e$ ). Both  $f_c$  and  $f_e$  are shown in gray scale. The velocity of the melt ( $\bar{u}_l$ ) is shown together with  $f_c$  a), while the velocity of the equiaxed crystals ( $\bar{u}_e$ ) is shown with  $f_e$  b). Some isolines of volume fraction of phases are marked, indicating the columnar tip front ( $f_c = 10^{-3}$ ), equiaxed packing bound ( $f_e = 0.19$ ), and in the mushy region ( $f_c = 0.2, 0.5$ ).

### 3. Summary, Discussion, and Outlook

The ultimate application goal of the numerical simulation for ingot casting is to realize the process design and optimization by improving soundness and homogeneity (both structural and compositional) of the ingot, minimizing the preparation and material costs, reducing energy loss, etc. Additionally, the simulation tools must be user-friendly and the input data for preparing the simulation must be manageable. By analyzing the simulation examples as presented in this article, this goal seems too ambitious for the time being. At least, it is not possible to have all the above features integrated into one simulation tool. Does this render the current simulation tools useless? On the contrary, the past modeling/simulation experience demonstrates the practical and potential significance of the following:

1. In the practice of ingot production, one often faces one or two mostly critical issues, for example, porosity. Other issues may concern tolerance of control. In this case, no comprehensive modeling tool is needed. A simplified tool by considering only the thermal field would be a reasonable choice. The simulation examples (Figure 2,3) show some success of this application. Today, many steel plants have such options with commercial tools like ProCAST<sup>[11]</sup> and MAGMA-SOFT.<sup>[12]</sup> Calculation cost and the knowledge demand for running such simulations is feasible.
2. Understanding the formation mechanisms of macrosegregation is still an active topic of research. The knowledge as developed from the previous experiments (no direct observation is possible) was indirectly derived without sound proofing, and they sometimes contradict each other. The solidification process (Figure 7,10) involves multiphase fluid mechanics and is much more complicated than presumed (Figure 5). The knowledge gained in the past is not sufficient for the purpose of making a quantitative prediction. The examples (Figure 6–10) demonstrated that being able to numerically “reproduce” the solidification and transport phenomena in real ingots is essential for understanding the formation mechanisms of macrosegregation. A live prediction can only be realistic when the laws of physics are considered in the model.
3. By developing multiphase solidification models, some important scientific topics have become the focus of attention in metallurgy. The macroscopic transport phenomena and the microscopic crystal growth kinetics must be bridged through many auxiliary models, which are available, but neither completed nor precise. They include the permeability laws for interdendritic flow, parameters to describe the dendritic growth kinetics (tracking the columnar tip front), origin of the equiaxed crystals by heterogeneous nucleation or crystal fragmentation, physical, and thermodynamic

properties, etc. If a comprehensive model has the ability to “reproduce” the ingot solidification, as seen in Figure 8–10, the studies on the aforementioned auxiliary models become practically significant, not only scientifically significant.

The four simulation examples as shown in this article target only the most serious issues of steel ingots, such as shrinkage porosity/cavity, thermal stress and strain and the formation of inner cracks, and different types of macrosegregation. Note, that some other issues have also been tackled by different modeling researchers, for example, non-metallic inclusions and influence on the macrosegregation,<sup>[79,80]</sup> cellular automata simulation of the macrosegregation,<sup>[81]</sup> interactions between thermal mechanics and fluid mechanics,<sup>[82–84]</sup> etc.

There is an inherent conflict with regard to a model's capacity and calculation efficiency. The capacity of an oversimplified model is definitely limited by its assumptions; while the simulation with fewer simplifications would require larger computational resources. A calculation time of several weeks would be beyond practical consideration. Table 1 lists the available macrosegregation models as developed in last decades. The first 2D simulation example for an industrial ingot with a mixture model was presented by Gu and Beckermann in 1999<sup>[47]</sup>; the 2D simulation example with a two-phase model was done by Combeau et al in 2009<sup>[72]</sup>; a full-3D simulation of an industrial ingot with a four-phase model, incorporating both shrinkage cavity and macrosegregation, was recently publicized by the current authors.<sup>[36]</sup> Following this development trend and according to the projection of Moore's law by Voller et al.,<sup>[85]</sup> the full 3D calculation of industry ingots with multiphase model will become practically feasible in foreseeable future.

Received: January 24, 2017;

Published online: April 13, 2017

**Keywords:** casting; cavity; ingot; macrosegregation; porosity; shrinkage; simulation

#### References

- [1] a) 1st Report on the heterogeneity of steel ingots, *J. Iron Steel Inst.* **1926**, *113*, 39. b) 2nd Report on the heterogeneity of steel ingots, *J. Iron Steel Inst.* **1928**, *117*, 401. c) 3rd Report on the heterogeneity of steel ingots, *J. Iron Steel Inst.* **1929**, *119*, 305.
- [2] E. Marburg, *J. Met.* **1953**, *5*, 157.
- [3] A. Kohn, *Iron Steel Inst. London* **1968**, *P110*, 356.
- [4] K. W. Andrews, C. R. Gomer, *Iron Steel Inst. London* **1968**, *P110*, 363.
- [5] G. Lesoult, *Mater. Sci. Eng. A* **2005**, *413–414*, 19.
- [6] J. Wang, P. Fu, H. Liu, D. Li, Y. Li, *Mater. Des.* **2012**, *35*, 446.

- [7] K. Kajikawa, S. Suzuki, F. Takahashi, S. Yamamoto, T. Suzuki, S. Ueda, T. Shibata, H. Yoshida, *1st Int. Conf. Ingot Casting, Rolling and Forging (ICRF)*, Aachen, Germany **2012**.
- [8] E. J. Pickering, C. Chesman, S. Al-Bermani, M. Holland, P. Davies, J. Talamantes-Silva, *Metall. Mater. Trans. B* **2015**, *46B*, 1860.
- [9] Z. Duan, W. Tu, B. Shen, H. Shen, B. Liu, *Metall. Mater. Trans. A* **2016**, *47A*, 3597.
- [10] R. Sevrin, *Mathematical models in metallurgical process development*, ISI Publication 123, The Iron and Steel Institute, **1970**, 147. ISBN 0900497114.
- [11] ProCAST, ESI Group, France **2015**.
- [12] MAGMASOFT v4.5, MAGMA GmbH, Aachen, Germany.
- [13] J. J. Moore, N. A. Shah, *Int. Met. Rev.* **1983**, *28*, 338.
- [14] I. Ohnaka, *Microsegregation and Macrosegregation*, ASM Handbook, 15–Casting, ASM Int., Metals Park, USA **1992**, p. 136.
- [15] M. C. Flemings, *ISIJ Int.* **2000**, *40*, 833.
- [16] C. Beckermann, *Int. Mater. Rev.* **2002**, *47*, 243.
- [17] D. J. Pickering, *ISIJ Int.* **2013**, *53*, 935.
- [18] A. Ludwig, M. Wu, A. Kharicha, *Metall. Mater. Trans. A* **2015**, *46A*, 4854.
- [19] I. Imafuku, K. Chijiwa, *AFS Trans.* **1983**, *91*, 527.
- [20] C. Pequet, M. Gremaud, M. Rappaz, *Metall. Mater. Trans. A* **2002**, *33A*, 2095.
- [21] E. Niyama, T. Uchida, M. Morikawa, S. Saito, *AFS Cast. Met. J.* **1982**, *7*, 52.
- [22] K. Carlson, C. Beckermann, *Metall. Mater. Trans. A* **2009**, *40*, 163.
- [23] K. Tashiro, S. Watanabe, I. Kitagawa, I. Tamura, *Trans. ISIJ* **1983**, *23*, 312.
- [24] S. Qian, X. Hu, Y. Cao, X. Kang, D. Li, *Mater. Des.* **2015**, *87*, 205.
- [25] P. Lan, J. Q. Zhang, *Ironmaking and Steelmaking* **2014**, *41*, 598.
- [26] L. Hartmann, C. Ernst, J. S. Klung, *IOP Conf. Series: Mater. Sci. Eng.* **2011**, *27*, <https://doi.org/10.1088/1757-899X/27/1/012063>
- [27] B. G. Thomas, I. V. Samarasekera, J. K. Brimacombe, *Metall. Trans. B* **1987**, *18B*, 131.
- [28] B. G. Thomas, I. V. Samarasekera, J. K. Brimacombe, *Metall. Trans. B* **1988**, *19B*, 277.
- [29] B. G. Thomas, I. V. Samarasekera, J. K. Brimacombe, *Metall. Trans. B* **1988**, *19B*, 289.
- [30] J. Yang, H. Shen, B. Liu, Y. Xu, Y. Hu, B. Lei, *China Foundry* **2016**, *13*, 191.
- [31] M. Bellet, O. Cerri, M. Bobadilla, Y. Chastel, *Metall. Mater. Trans. A* **2009**, *40A*, 2705.
- [32] T. Koshikawa, M. Bellet, C.-A. Gandin, H. Yamamura, M. Bobadilla, *Metall. Mater. Trans. A* **2016**, *47A*, 4053.
- [33] T. Clyne, G. Davies, *Solidification and Casting of Metals*, TMS, Warrendale, PA **1977**, p. 275.
- [34] Y. Won, T. Ye, D. Seol, K. Oh, *Metall. Mater. Trans. B* **2000**, *31B*, 779.
- [35] M. Bellet, V. Fachinotti, *Comput Methods Appl. Mech. Eng.* **2004**, *193*, 4355.
- [36] M. Wu, A. Ludwig, A. Kharicha, *Appl. Math. Modell.* **2017**, *41*, 102.
- [37] M. C. Flemings, G. E. Nereo, *Trans. AIME* **1967**, *239*, 1449.
- [38] W. D. Bennon, F. P. Incropera, *Int. J. Heat Mass Transfer* **1987**, *30*, 2161.
- [39] C. J. Vreeman, M. J. M. Krane, F. P. Incropera, *Int. J. Heat Mass Transfer* **2000**, *43*, 677.
- [40] V. R. Voller, C. Prakash, *Int. J. Heat Mass Transfer* **1987**, *30*, 1709.
- [41] V. R. Voller, A. D. Brent, C. Prakash, *Int. J. Heat Mass Transfer* **1989**, *32*, 1719.
- [42] V. R. Voller, A. D. Brent, C. Prakash, *Appl. Math. Model.* **1990**, *14*, 320.
- [43] V. R. Voller, C. R. Swaminathan, *Numer. Heat Transfer Part B* **1991**, *19*, 175.
- [44] P. J. Prescott, F. P. Incropera, *Transport Phenomena in Materials Processing Manufacturing*, ASME HTD **1994**, *280*, 59.
- [45] P. J. Prescott, F. P. Incropera, *J. Heat Transfer* **1994**, *116*, 735.
- [46] P. J. Prescott, F. P. Incropera, D. R. Gaskell, *J. Heat Transfer* **1994**, *116*, 742.
- [47] J. P. Gu, C. Beckermann, *Metall. Mater. Trans. A* **1999**, *33*, 1357.
- [48] M. Krane, F. Incropera, D. Gaskell, *Int. J. Heat Mass Transfer* **1997**, *40*, 3827.
- [49] M. Schneider, C. Beckermann, *Metall. Mater. Trans. A* **1995**, *26*, 2373.
- [50] M. Rappaz, *Int. Mater. Rev.* **1989**, *34*, 93.
- [51] C. Beckermann, R. Viskanta, *Appl. Mech. Rev.* **1993**, *46*, 1.
- [52] J. Ni, C. Beckermann, *Metall. Mater. Trans. B* **1991**, *22*, 349.
- [53] A. Ludwig, M. Wu, *Metall. Mater. Trans. A* **2002**, *33*, 3673.
- [54] M. Wu, A. Ludwig, A. Bührig-Polaczek, M. Fehlbier, P. R. Sahm, *Int. J. Heat Mass Transfer* **2003**, *46*, 2819.
- [55] M. Wu, A. Ludwig, *Adv. Eng. Mater.* **2003**, *5*, 62.
- [56] T. Wang, S. Yao, X. Zhang, J. Jin, M. Wu, A. Ludwig, B. Pustal, A. Bührig-Polaczek, *ACTA Metall. Sin.* **2006**, *42*, 584.
- [57] M. Wu, A. Ludwig, J. Luo, *Mater. Sci. Forum* **2005**, *475–479*, 2725.
- [58] K. Miyazawa, K. Schwerdtfeger, *Arch. Eisenhüttenwes* **1981**, *52*, 415.
- [59] T. Kajitani, J. M. Drezet, M. Rappaz, *Metall. Mater. Trans. A* **2001**, *32*, 1479.
- [60] H. Combeau, M. Bellet, Y. Fautrelle, D. Gobin, E. Arquis, B. Budenkova, B. Dussoubs, Y. Terrail, A. Kumar, Ch.-A. Gandin, B. Goyeau, S. Mosbah, T. Quatrevaux, M. Rady, M. Zaloznik, *McWASP XIII IOP Conf. Series: Mater. Sci. Eng.* **2012**, *33*, eds. A. Ludwig, M. Wu, A. Kharicha, <https://doi.org/10.1088/1757-899X/33/1/012086>

- [61] M. Wu, L. Könözsy, A. Ludwig, W. Schützenhöfer, R. Tanzer, *Steel Res. Int.* **2008**, 79, 637.
- [62] F. Mayer, M. Wu, A. Ludwig, *Steel Res. Int.* **2010**, 81, 660.
- [63] M. Wu, J. Domitner, A. Ludwig, *Metall. Mater. Trans. A* **2012**, 43, 945.
- [64] J. Li, M. Wu, J. Hao, A. Ludwig, *Comp. Mater. Sci.* **2012**, 55, 407.
- [65] J. Li, M. Wu, J. Hao, A. Kharicha, A. Ludwig, *Comp. Mater. Sci.* **2012**, 55, 419.
- [66] M. Wu, A. Ludwig, *Mater. Sci. Eng. A* **2005**, 413–414, 192.
- [67] M. Wu, A. Ludwig, *Metall. Mater. Trans. A* **2006**, 37, 1613.
- [68] M. Wu, A. Ludwig, *Metall. Mater. Trans. A* **2007**, 38A, 1465.
- [69] J. Li, M. Wu, A. Kharicha, A. Ludwig, *Int. J. Heat Mass Transfer* **2014**, 72, 668.
- [70] M. Wu, J. Li, A. Kharicha, *Comp. Mater. Sci.* **2013**, 79, 830.
- [71] M. Wu, J. Li, A. Kharicha, A. Ludwig, *Comp. Mater. Sci.* **2014**, 92, 267.
- [72] H. Combeau, M. Zaloznik, S. Hans, P. E. Richey, *Metall. Mater. Trans. B* **2009**, 40B, 289.
- [73] Z. Duan, W. Tu, B. Shen, H. Shen, B. C. Liu, *Metall. Mater. Trans. A* **2016**, 47A, 3597.
- [74] W. Tu, Z. Duan, B. Shen, H. Shen, B. C. Liu, *JOM* **2016**, 68, 3116.
- [75] M. G. Worster, *Ann. Rev. Fluid Mech.* **1997**, 29, 91.
- [76] C. Beckermann, J. P. Gu, W. J. Boettinger, *Metall. Mater. Trans. A* **2000**, 31A, 2545.
- [77] K. Suzuki, T. Miyamoto, *Tetsu-to-Hagane (J. Iron Steel Inst. Jpn)* **1977**, 63, 45.
- [78] M. Zaloznik, H. Combeau, *Int. J. Therm. Sci.* **2010**, 49, 1500.
- [79] D. Li, X. Chen, P. Fu, X. Ma, H. Liu, Y. Chen, Y. Cao, Y. Luan, Y. Li, *Nat. Comm.* **2014**, 5, 5572. <https://doi.org/10.1038/ncomms6572>.
- [80] Y. Cao, Y. Chen, D. Li, *Acta Mater.* **2016**, 107, 325.
- [81] P. Lan, H. Tang, J. Zhang, *Metall. Mater. Trans. A* **2016**, 47A, 2964.
- [82] M. Bellet, O. Cerri, M. Bobadilla, Y. Chastel, *Metall. Mater. Trans. A* **2009**, 40A, 2705.
- [83] M. Bellet, O. Boughanmi, G. Fidel, *IOP Conf. Series: Mater. Sci. Eng.* **2012**, 33, <https://doi.org/10.1088/1757-899X/33/1/012052>
- [84] A. Ludwig, A. Vakhrushev, M. Wu, T. Holzmann, *Trans. Indian Inst. Met.* **2015**, 68, 1087.
- [85] V. Voller, F. Porte-Agel, *J. Comp. Phys.* **2002**, 179, 698.